AIAA Propulsion and Energy Forum
19-22 August 2019, Indianapolis, IN
AIAA Propulsion and Energy 2019 Forum

10.2514/6.2019-3933

Check for updates

Supercritical GN_2/GH_2 jet modeled by the ECS method

Wei Yao[1] Yichao Jin[2] and Yachao Lee[3]
Key Laboratory of High-Temperature Gas Dynamics, Institute of Mechanics, CAS, Beijing 100190, China
School of Engineering Science, University of Chinese Academy of Science, Beijing 100049, China

In the framework of large eddy simulation, a supercritical GN_2/GH_2 jet has been modeled by using the ECS method, whose accuracy has been verified for a binary N_2/H_2 mixture against the standard data. A hydrid pressure/density solver is developed to model the high-speed flow caused by the sudden volume expansion of a heated flow in case of the stiff phase-change phenomenon. Grid convergence study was conducted for mesh resolutions from 9.6 to 20.02 million cells. In comparison with the experimental data, the current prediction overpredicts the potential core of the nitrogen jet, while agrees better in the fully mixing region. A waist-like region can be identified as a relatively higher density overlaid on a lower density region, which is observed to be not an instantaneous phenomenon. A mushroom-cap region is formed when the thermal expansion rate of nitrogen jet has a sudden increase due to the breakup of the jet potential core. The drastic expansion obviously increases transverse velocity, which causes an obvious increase in the width of the jet flow. The streamlines indicate that the flow turns transversely at the location corresponding to the sudden expansion region, and it is the backflow causes the shrinking waist-like region.

Nomenclature

P	=	pressure
ρ	=	density
T	=	temperature
u_i	=	velocity in x_i direction
τ_{ij}	=	viscous stress tensor
H	=	enthalpy
Y_α	=	mass fraction of species α
D_α	=	equivalent mass diffusion coefficient
x_α	=	mole fraction of species α
D_T	=	thermal diffusivity
Ψ_T	=	turbulent enthalpy flux
Ψ_α	=	turbulent species diffusion
C_p	=	pressure coefficient
v	=	viscosity
D	=	diameter
S	=	strain rate tensor
Q	=	Q-criterion
Pr_t	=	turbulent Prandtl number
Sc_t	=	turbulent Schmidt number
t	=	time
x, y, z	=	Cartesian coordinates

Superscripts

—	=	cell average

[1] Associate Professor, Institute of Mechanics (CAS), weiyao@imech.ac.cn, AIAA member (Corresponding author).
[2] PHD student, Institute of Mechanics (CAS), tdxh1993@buaa.edu.cn
[3] PHD student, Institute of Mechanics (CAS), liyachao@imech.ac.cn

~ = Favre average

sgs = subgrid-scale

I. Introduction

The thermodynamic and transport properties, such as density, enthalpy, and viscosity of trans- or supercritical fluids differ significantly with those at subcritical states and can have important impacts on the flow and heat transfer, which then often leads to a series of abnormal phenomena. In the early studies, heat transfer enhancement or deterioration has been frequently observed under supercritical pressures due to the variable property effect, buoyancy effect, and thermal-induced acceleration effect [1]. Supercritical flow instabilities [2-7] is another critical problem that has been investigated by many researchers. The instability of flow and heat transfer often occurs in cooling equipment with two phases or supercritical states. It is generally believed that the acute variation of density near the pseudo-critical temperature is one of the main factors leading to flow instabilities [7].

The phase change is a dynamic equilibrium process relating to remarkable pressure variation if the volume is constrained, e.g., in a tube or chamber. For example, the high-pressure cryogenic liquid commonly used in rocket engines can expand dramatically in the combustion chamber due to the receiving of extremely high heat flux. Under such circumstances, a stiff phase-change phenomenon will occur if the time for phase change is extremely short. The acute phase change, usually due to severely heated evaporation/expansion, is often exhibited as weakly compressible flows with dramatic property change. The low-speed expansion can always be safely approximated as an isobaric process, which however cannot be assumed when the Mach number driven by the expansion exceeds 0.3. In nearly quiescent flows, a severe phase change can even produce a local supersonic phenomenon, which would further produce local lower pressure and affect the phase change process.

The difficulties in the measurement of flow fields at supercritical pressure result in a poor understanding in the fluid mechanics of supercritical flows [8], making the use of computational fluid dynamics (CFD) attractive for the complementary analysis of supercritical flows.

However, it must be admitted that accurate modeling of supercritical flows is also technically challengeable due to the phase-change stiffness and extremely high Reynolds number caused by the drastic changes in properties (especially the density), as well as the strong coupling between the fluids at different phase states. Special attention should be paid in the modeling of stiff phase-change phenomenon on the following aspects, 1) real-gas effect, 2) adaptative time step and grid sizes, 3) numerical schemes with good robustness and low dissipation, and 4) compressible turbulence-related models, and

Cubic equations of state (EoSs) has been widely used to describe the real-gas effect due to their simplicity. For example, Peng-Robinson (PR) [9,10] and Soave-Redlich-Kwong (SRK) [9] equation of state were used to simulate supercritical fluid injection. Although with the advantage of high computational efficiency, the cubic EoSs are inaccurate under certain conditions, such as vapor-liquid equilibria or near-critical regions [11]. Oefelein [12] pointed out that the SRK equation performs better at low temperatures, while the PR equation is more suitable in reacting flows involving heat release. Bonelli et al. [13] simulated a highly unexpanded hydrogen jet under the supercritical condition and showed that evident differences exist for the predictions of the jet structures given by the ideal gas law, the Van-Der-Waals equation, and the Redlich-Kwong equation.

An accurate description of the nonlinear thermodynamic properties is the key to simulate the phase-change flow process. According to the fact that the state curves of different fluids are similar, one feasible method to acquire an unknown state is through the state variable scaling and similarity transformations based on the known state, i.e., the principle of Extended Corresponding States (ECS) [14,15]. Compared with the cubic EoSs, the ECS method can predict the thermodynamic nonidealities and transport anomalies over a wide range of states. Previous studies [16,17] have shown that the ECS method can accurately and economically describe the properties of a supercritical fluid.

II. Physical models and numerical methods

A. Experimental case

In the present study, large eddy simulation (LES) coupled with the ECS method is used to simulate the realistic pressure-temperature-density behavior of coaxial liquid nitrogen and preheated gaseous hydrogen (LN2/GH2) injection at supercritical pressures. The schematic of the computational domain is shown in Figure 1. In order to reproduce the experiment result of Oschwald et al. [18] and the numerical result of Müller et al. [10]. Cryogenic nitrogen is injected through the inner tube of a coaxial injector into a tank filled with nitrogen at supercritical pressure and ambient temperature, while hydrogen is injected through an annulus. The diameter of the nitrogen injector is 2.4 mm, and the annulus width of the hydrogen injector is 0.5 mm. The initial temperature of supercritical nitrogen is 158.8 K, and the hydrogen has been preheated to 270 K. Both of them are injected at a pressure of 4 MPa. The initial velocities are 5 m/s and 60 m/s respectively for the nitrogen and hydrogen jets. The tank filled with nitrogen maintained at 4 MPa and 300 K through replenishing preheated nitrogen continuously. The nitrogen density at the injector exit is 150.7 kg/s, which is much higher than the hydrogen density of 3.5 kg/s. Accordingly, the designed momentum ratio of nitrogen-to-hydrogen is 3.34. Note the critical point for nitrogen is 126.21 K and 3.39 MPa, while 32.938 K and 1.2858 MPa for hydrogen, thus both the nitrogen and hydrogen jets is injected at the supercritical status and will be maintained at due to the fact that the tank pressure is well above their critical pressures. The case is indeed a mixing problem between twin supercritical streams.

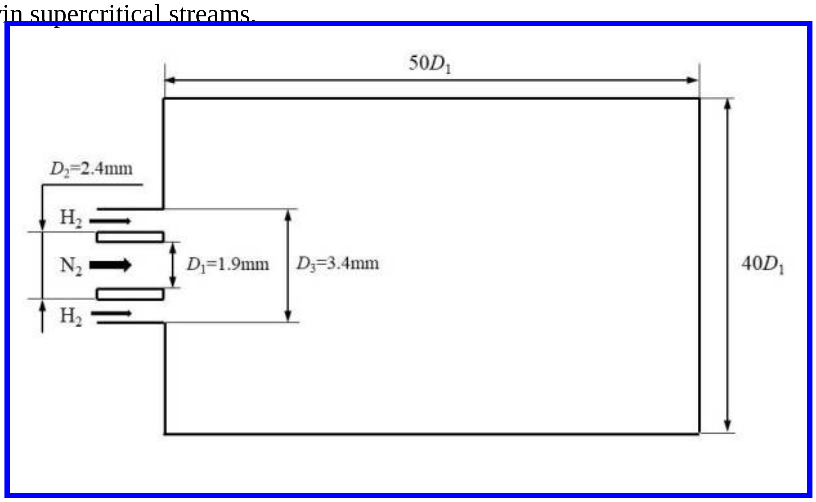

Figure 1. Schematic of the computational domain

B. Governing equations

The unsteady and three-dimensional Favre-averaged compressible Navier-Stokes equations (NSE) are solved for a set of conservative variables ($\bar{\rho}$, $\tilde{u}_i$, $\widetilde{H}_t$, $\widetilde{Y}_\alpha$),

$$\frac{\partial\bar{\rho}}{\partial t}+\frac{\partial\bar{\rho}\tilde{u}_j}{\partial x_j}=0 \tag{1}$$

$$\frac{\partial\bar{\rho}\tilde{u}_i}{\partial t}+\frac{\partial\bar{\rho}\tilde{u}_j\tilde{u}_i}{\partial x_j}+\frac{\partial\bar{p}}{\partial x_i}-\frac{\partial\tilde{\tau}_{ij}}{\partial x_j}=-\frac{\partial\tau_{ij}}{\partial x_j} \tag{2}$$

$$\frac{\partial\bar{\rho}\widetilde{H}_t}{\partial t}+\frac{\partial\bar{\rho}\tilde{u}_j\widetilde{H}_t}{\partial x_j}-\frac{\partial}{\partial x_j}\left(\bar{\rho}D_T\frac{\partial\widetilde{H}_t}{\partial x_j}+\sum_{\alpha=1}^{L}\bar{\rho}D_\alpha\frac{\partial\widetilde{Y}_\alpha}{\partial x_j}\widetilde{H}_\alpha\right)-\frac{\partial\bar{p}}{\partial t}-\frac{\partial\tilde{u}_j\tilde{\tau}_{ij}}{\partial x_j}=-\frac{\partial\Psi_{T,j}}{\partial x_j} \tag{3}$$

$$\frac{\partial\bar{\rho}\widetilde{Y}_\alpha}{\partial t}+\frac{\partial\bar{\rho}\tilde{u}_j\widetilde{Y}_\alpha}{\partial x_j}-\frac{\partial}{\partial x_j}\left(\bar{\rho}D_\alpha\frac{\partial\widetilde{Y}_\alpha}{\partial x_j}\right)=-\frac{\partial\Psi_{\alpha,j}}{\partial x_j} \tag{4}$$

$$\bar{p}=\bar{\rho}R\widetilde{T} \tag{5}$$

$$\widetilde{H}_t=\widetilde{H}+\frac{1}{2}\tilde{u}_i\tilde{u}_i=\widetilde{H}^0+\int_0^T C_p dT+\frac{1}{2}\tilde{u}_i\tilde{u}_i \tag{6}$$

Here the bar "-" and the tilde "~" represent averaged and Favre-averaged quantities respectively, t denotes the time, x_i is the Cartesian coordinate in direction i, $\bar{\rho}$ is the density, $\tilde{u}_i$ is the velocity component in x_i direction (spatial dimension i = 1, 2, 3), $\bar{p}$ is the pressure, $\tilde{\tau}_{ij}$ is the viscous stress tensor, $\widetilde{H}_t=\widetilde{H}+0.5\tilde{u}_i^2$ is the total absolute enthalpy obtained as the sum of the absolute enthalpy $\widetilde{H}$ and the resolved kinetic energy, the absolute enthalpy $\widetilde{H}$ is calculated as the sum of the formation enthalpy $\widetilde{H}^0$ at standard reference state and the sensible enthalpy change from the reference temperature to T, $\widetilde{Y}_\alpha$ is the mass fraction of species α (α = 1 , ..., L, with L the total species number), the specific heat C_p is a function of species concentrations and temperature, $\bar{\omega}_\alpha$ is the averaged mass production rate of chemical species α in the unit of $kg\cdot m^{-3}\cdot s^{-1}$, D_α is mixture-averaged mass diffusivity of species α, D_T is the thermal diffusivity, $\widetilde{T}$ is the temperature, $R=R_u/W$ is the gas constant, $R_u=8.314\,J\cdot mol^{-1}\cdot K^{-1}$ is the universal gas constant, $W=(\sum_{\alpha=1}^{L}Y_\alpha/W_\alpha)^{-1}$ is the molar weight of the multicomponent mixture. According to the Stokes's hypothesis which ignoring the bulk viscosity, the shear-stress tensor for a Newtonian fluid is calculated as:

$$\tilde{\tau}_{ij} = \bar{\rho}\nu(\tilde{T})\left(2\tilde{S}_{ij} - \tfrac{2}{3}\delta_{ij}\tilde{S}_{kk}\right) \tag{7}$$

where ν is a temperature-dependent kinetic viscosity and the rate-of-strain tensor of the resolved scales is calculated as:

$$\tilde{S}_{ij} = \tfrac{1}{2}\left(\frac{\partial \tilde{u}_i}{\partial x_j} + \frac{\partial \tilde{u}_j}{\partial x_i}\right) \tag{8}$$

The thermodiffusion (Soret effect), barodiffusion and mass-driven diffusion of heat (Dufour effect) are ignored in Eqs. (3)-(4).

The turbulent Reynolds stresses (τ_{ij}) and turbulent fluxes ($\Psi_{T,j}$ and $\Psi_{\alpha,j}$) in Eqs. (1)~(6) are unclosed and both require specific modeling. The Reynolds stress, defined as $\tau_{ij} = \bar{\rho}\left(\widetilde{u_i u_j} - \tilde{u}_i\tilde{u}_j\right)$, is modeled by the Boussinesq eddy viscosity hypothesis, where the Reynolds stresses are also taken to be proportional to $\tilde{S}_{ij}$,

$$\tau_{ij} = \underbrace{\left(\tau_{ij} - \tfrac{1}{3}\delta_{ij}\tau_{kk}\right)}_{deviatoric} + \underbrace{\tfrac{1}{3}\delta_{ij}\tau_{kk}}_{isotropic} = -\bar{\rho}\nu_t\left(2\tilde{S}_{ij} - \tfrac{2}{3}\delta_{ij}\tilde{S}_{kk}\right) + \tfrac{2}{3}\delta_{ij}\bar{\rho}k_t \tag{9}$$

Here ν_t is the eddy viscosity given by the specified turbulence model, k_t is the unresolved turbulent kinetic energy. Because $\tau_{kk} = \gamma Ma_t^2\bar{p}$, with γ specific heat ratio, Ma_t unresolved Mach number and $\bar{p}$ filtered pressure, the isotropic term in Eq (9) is expected to be small for weakly compressible flows and can be safely neglected when the turbulent Mach number of the flow is small.

The turbulent enthalpy flux term $\Psi_{T,j} = \bar{\rho}\left(\widetilde{u_j H_t} - \tilde{u}_j\widetilde{H}_t\right)$ is modeled by the gradient diffusion assumption as

$$\Psi_{T,j} = -2\bar{\rho}\frac{\nu_t}{Pr_t}\frac{\partial \widetilde{H}_t}{\partial x_j} \tag{10}$$

where Pr_t is the turbulent Prandtl number. The turbulent species diffusion term $\Psi_{\alpha,j} = \bar{\rho}\left(\widetilde{u_j Y_\alpha} - \tilde{u}_j\tilde{Y}_\alpha\right)$ is also modeled using the gradient diffusion assumption as

$$\Psi_{\alpha,j} = -2\bar{\rho}\frac{\nu_t}{Sc_t}\frac{\partial \tilde{Y}_\alpha}{\partial x_j} \tag{11}$$

where Sc_t is the turbulent Schmidt number. Unity Pr_t and Sc_t are used in this study.

C. Property modeling

Figure 2 compares the density ρ, specific heat C_p, enthalpy h, and viscosity μ predicted by ECS and PR-EOS in comparison to the reference data from NIST [1]. The properties were calculated under constant pressure p=4 MPa for T=100 K, 120 K and 140 K respectively. The agreements are in general good for both ECS and PR-EOS, however, the ECS method provides better agreements for the density predictions. The ECS method well predict the density under all the three temperatures, while the PR-EOS model overpredicts the density at higher N_2 concentration for 100 K. The two peaks in the specific heat predictions correspond to the liquid-vapor equilibrium status, where slightly larger discrepancies occur for both the predictions of density and specific heat. For the cold nitrogen temperature of 158.8 K examined in this study, the gas is in supercritical status with only the vapor phase need to be considered in the modeling. The current ECS method shows a good capability to describe the gas status and phase properties.

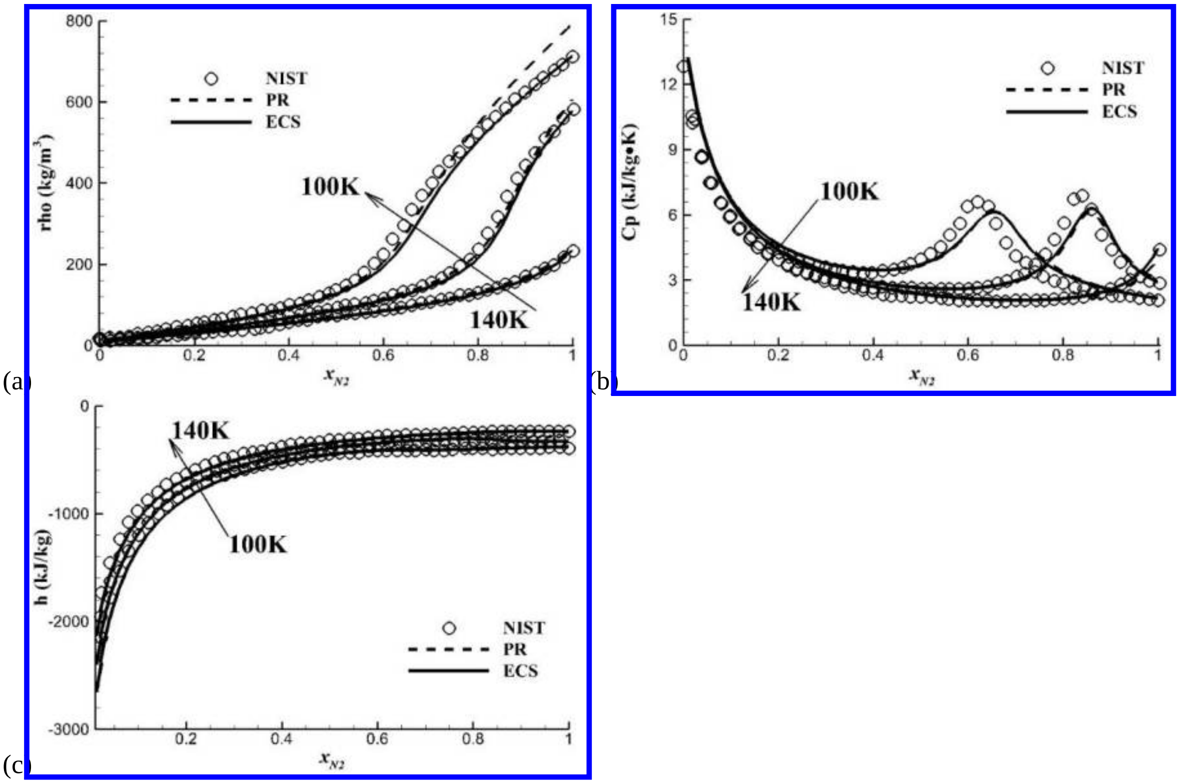

Figure 2. Verification of the real-gas thermodynamics model for a binary N_2/H_2 mixture at p=4 MPa

D. Turbulence model

To better capture the non-equilibrium kinetic energy transfer in the jet shear layer under high thermal expansion, the dynamic subgrid kinetic energy model (DKEM) [2] is used to model the subgrid-scale (SGS) turbulence effect. DKEM is developed by parameterizing the one-equation turbulent kinetic energy model [3, 4] using the resolved velocity scales. Through accounting for the non-local, historical and non-equilibrium transfer of the turbulence kinetic energy defined as $k_t = 0.5(\overline{u_k^2} - \bar{u}_k^2)$, between the grid-filter scale and the smaller subgrid dissipation scales, it is shown that [5-8] the one-equation model has advantages in modeling non-equilibrium turbulent dissipation and capturing fine-level fluctuation properties compared to some algebraic models (e.g., Smagorinsky model [9]). The following governing equations are employed,

$$\frac{\partial \bar{\rho} k_t}{\partial t} + \frac{\partial \bar{\rho} \tilde{u}_j k_t}{\partial x_j} = \frac{\partial}{\partial x_j}\left[\bar{\rho}\left(\frac{\nu_t}{Pr_t} + \frac{\nu}{Pr}\right)\frac{\partial k_t}{\partial x_j}\right] - \tau_{ij}^{sgs}\frac{\partial \tilde{u}_i}{\partial x_j} - C_\varepsilon \frac{\bar{\rho}(k_t)^{3/2}}{\bar{\Delta}} \tag{12}$$

$$\nu_t = C_\nu \bar{\Delta}\sqrt{k_t} \tag{13}$$

where C_ε and C_ν are model coefficients that will be determined dynamically [10, 11], and $\bar{\Delta}$ is the SGS filter width equal to the local grid dimension $V^{1/3}$ with V the cell volume, and laminar Prandtl number Pr=1. The dynamic determination of the model coefficients is based on the hypothesis that there is a significant correlation between the subgrid-scale stress τ_{ij} and the subtest-scale Leonard stress L_{ij} [12].

E. Solver and numerical methods

The governing equations are solved by an in-house developed finite-volume compressible LES solver AstroFoam, which is extended from the standard compressible solver rhoCentrolFoam distributed with the open-source CFD package OpenFOAM V3.0.1 [13] mainly by adding the modules of species transportation and chemical reaction with realistic thermodynamics and transport properties. The nonlinear inviscid convective fluxes are evaluated by using a second-order semi-discrete central Kurganov-Tadmor (KT) scheme [14]. A third-order spatial accuracy in reconstructing primitive convective fluxes at faces is achieved by the scale-selective discretization (SSD) scheme [15]. Temporal integration is advanced by the second-order Crank-Nicholson scheme [16]. The accuracy of AstroFoam has been extensively validated for various supersonic frozen flows [8, 17-23] and supersonic combustions [24-31].

In this study, the AstroFoam has been extended to model subsonic flows based on a hybrid method to solve and operate for a wide range of flow conditions. The original AstroFoam is a density-based solver suitable for high-speed compressible flows. In some cases, there is a large extent of subsonic flow coexists in the same domain. A pressure-based solver is added for low-speed incompressible flows. The pressure-based and density-based solvers are highly coupled through a threshold value, varying which from 0 to 1 will change the flow solver from the pressure-based to the density-based solver. The main difference between the pressure-based and the density-based algorithms lies in the calculation method of the inviscid flux, which is evaluated by the Kurganov-Tadmor (KT) scheme [14] in the density solver while the second-order central scheme in the skew-symmetric form [32] in the pressure-based solver. In the subsequent procedure, the pressure field is obtained based on gas law from the density field in the density-based solver while by solving a continuity-momentum coupled Poisson equation in the pressure-based solver. The time step is determined from the inviscid flux based on a maximum CFL (Courant) number, implying that the time step is mostly constrained by the density-based solver since its time step is much smaller than that in the pressure-based solver. The domain is firstly divided into several zones, within which the local maximum Mach number is calculated. A local maximum Mach number exceeding 0.3 will tune the solver into a density-based solver, whereas a pressure-based solver. The hybrid pressure/density is developed to model the high-speed flow caused by the sudden volume expansion of a heated flow, in case of the stiff phase-change phenomenon.

Multi-block mesh with axisymmetric (O-grid) pattern is used to mesh the whole domain, as shown in Figure 3. The mesh is clustered along the jet shear layer and the jet base to better capture the flow structures, while the coarser mesh is used in the far fields to reduce the computational cost as well as to avoid wave reflections. In order to examine the grid convergence, three different levels of mesh resolutions respectively with 9.6 M, 13.25 M, 15.85 M, and 20.02 M cells are investigated. The meshing details are summarized in Table 1. From the coarsest to the finest meshes, cell size in the streamwise direction reduces from 0.03 mm to 0.008 mm, while the radial cell size near the jet axis also reduces from 0.01 mm to 0.008 mm.

Table 1. Summary of the mesh configurations

Grid resolution		**Total grid number**
Streamwise (Δ_{min}/mm)	Radial (Δ_{min}/mm)	
0.03	0.01	9.60 Million
0.02	0.01	13.25 Million
0.01	0.008	15.85 Million
0.008	0.008	20.02 Million

The boundary conditions are configured to mimic the experimental conditions. The nitrogen and hydrogen jets are surrounded by ambient air, thus the open boundary condition is applied for the base, lateral and outlet sides, where a fixed chamber pressure of 4 MPa is specified and the velocity is determined by specifying a zero-gradient condition for outflow and constraining the inflow flux to satisfy the local mass conservation. During the modeling, the chamber pressure is maintained around 4 MPa, and the nitrogen replenished from the ambient with a temperature of 300 K sustains the chamber temperature to be a nearly constant 300 K.

The parallel computations are performed at the national supercomputer center in Tianjin (TH-1) using 112 CPU cores (Intel(R) Xeon(R) CPU E5-2690v4 with the base frequency of 2.60GHz). The time step is limited both by a maximum Courant number of 0.3 and a user-specified maximum time step of 2×10^{-8} s. The flush through time (FTT) defined based on the length of the combustor flow-path length (0.1 m) and the inlet flow speed of the hydrogen jet (60 m/s) is $1.67\times10^{-3}\ s$, and at least 3 FTTs (≈5 ms) are ensured for a meaningful data sampling and statistics.

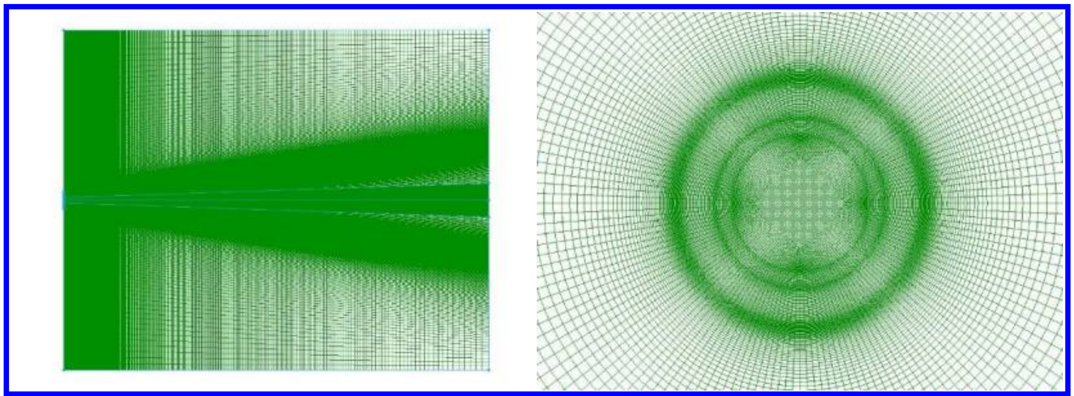

(a) (b)

Figure 3. Computational grid: (a) view of streamwise; (b) partially enlarged view at the inlet

III. Results and discussion

Figure 4 (a) shows the mean density predictions along the centerline by the four different mesh sets with 9.6 million, 13.25 million, 15.85 million and 20.02 million cells. The small discrepancies between the results given by different meshes indicate that gird dependence has been achieved. Figure 4 (b) shows the relative error calculated from the absolute deviations from the finest result as $|\rho - \rho_{2.02}|/\rho_{2.02}$. As the mesh is refined from 9.6 M to 15.85 M, the mean relative error reduces from 1.38%, 1.24 to 1.16%, indicating the trend of grid convergence. In the following analysis, the finest mesh with 20.02 M cells is used since more flow details have been directly resolved in the LES framework.

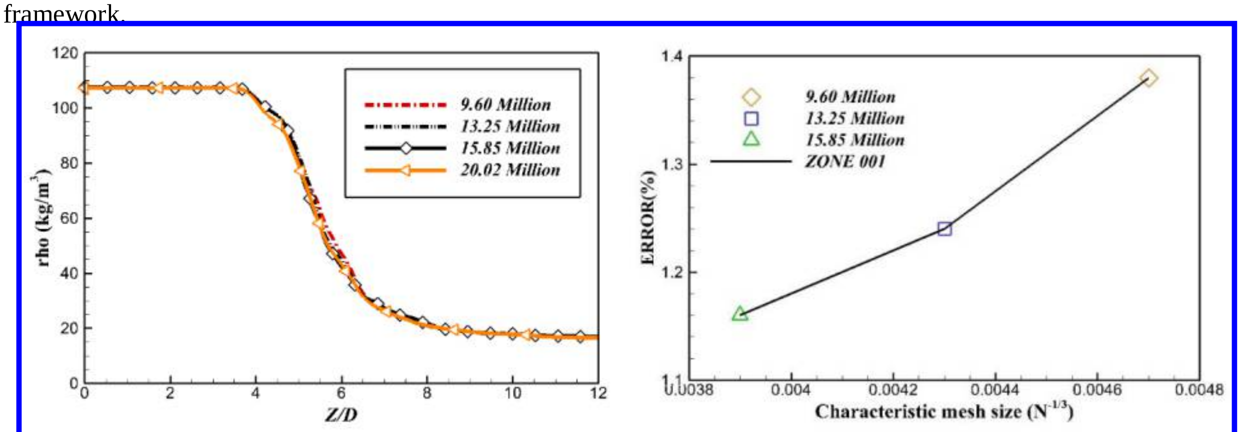

(a) (b)

Figure 4. (a) Axial density predictions and (b) relative errors under 4 mesh resolutions

A comparison of the LES results with the experimental measurements for the averaged hydrogen and nitrogen density on the jet centerline is shown in Figure 5. The experimental data for the nitrogen density exhibit a plateau before the breakup of the jet potential core, indicating that the length of the cryogenic potential core is around 2*D* (0 < *Z/D* <2). This jet potential core, however, has been doubly overpredicted to be 4*D* in the current modeling. And after being thoroughly mixed in the downstream since *Z/D*=6, the fluid density approaches a stable value. The prediction agrees better in the fully mixing region. Since the jet breakup is largely influenced by the vast density variation caused by thermal expansion in the examined case, an improvement in the heat transfer model including real-gas effect should be able to produce smaller discrepancy.

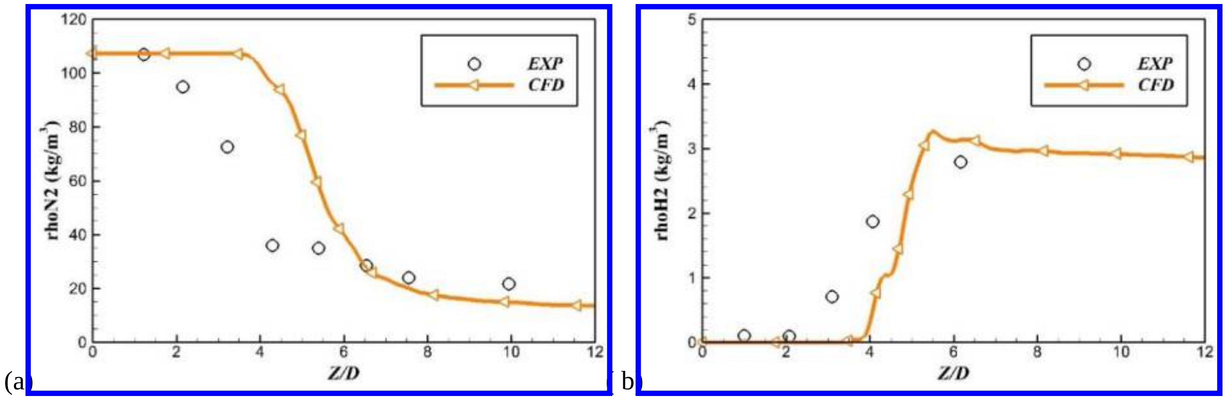

Figure 5. Axial variations of (a) nitrogen density and (b) hydrogen density

Figure 6 shows the instantaneous distributions of hydrogen and nitrogen on the centerplane. The hydrogen jet disperses quickly within an axial distance of 2*D* if defining the potential core by mass fraction higher than 0.9. The main core of the nitrogen jet persists until around Z=6*D*, before which the mixing between the hydrogen and the nitrogen is dominated by the small eddies arisen from the shear stress. After Z=6*D* and within a short axial distance of 2*D*, the nitrogen jet breaks up into discrete "droplet-shape" regions, which then quickly vanished. After Z=8*D*, the hydrogen and nitrogen streams visually mixed completely. From the distribution of both nitrogen and hydrogen concentrations, the width of the mixing plume reaches its maximum at Z=8*D*, and then decrease almost linearly with the axial distance until Z=17*D*, where a narrow waist-like region can be observed in the mixing plume.

Figures 7 and 8 show the instantaneous temperature and density contours on the centerplane. The nitrogen jet with low temperature is surrounded by a warm mixing layer and is gradually heated from the core temperature of 158.8 K to the ambient temperature of 300 K. The width of cold nitrogen jet shrinks due to the thermal "erosion" of the warm hydrogen coflow, and the final drastic breakup occurs from Z=6-8D. Unlike the species diffusion, the thermal diffusion is more obvious for the hydrogen jet, as the outer jet width, delimited for example by 280 K from the surrounding ambient nitrogen with 300 K, increases almost linearly until Z=7D. An observable temperature difference between the nitrogen stream and the hydrogen stream along the axis exists until Z=12D. The density depends on both the temperature and the molecular weight. A slightly thinner nitrogen jet core delimited by the exit value of the nitrogen density is observed in comparison with that delimited by a critical temperature of 160 K, indicating that the thermal diffusion is faster than the species diffusion and the non-unity Lewis number effect should be considered in this case. In the outer edge of the plume, although the temperature difference between the plume and the surrounding ambient nitrogen is small, an obvious interface delimited by density between them can be observed. From the nitrogen density in Figure 8 (c), the mixing between the hydrogen and the ambient nitrogen is generally slow, and a clear interface can be still observed until the chamber outlet at Z=26*D*. From the hydrogen density distribution, the waist-like region can be clearly identified as a relatively higher density overlaid on a lower density region.

Figure 9 shows the instantaneous vortex structures colored by the temperature at a time interval of 1×10^{-4} s. The vortex structures are similar at different times. The time interval corresponds to the period of a lateral oscillation of the potential core of the nitrogen jet. As seen, the waist-like region exists in all the sequent images and thus is not an instantaneous phenomenon. Based on this waist-like region, the jet flow can be divided into two stages, the development jet region before Z=17*D* and the fully-mixing plume region after that. Fine vortex structures start to fall off from the jet body after Z=30*D*, and few vortex structures can be observed in the resolved scale after Z=42*D*. The jet flow has an increasing temperature from the core to the outer layer. Judging from the consistency of the surface temperature, part of those fine vortex structures are broken from the outer layer, while the rest are broken directly from the inner layer.

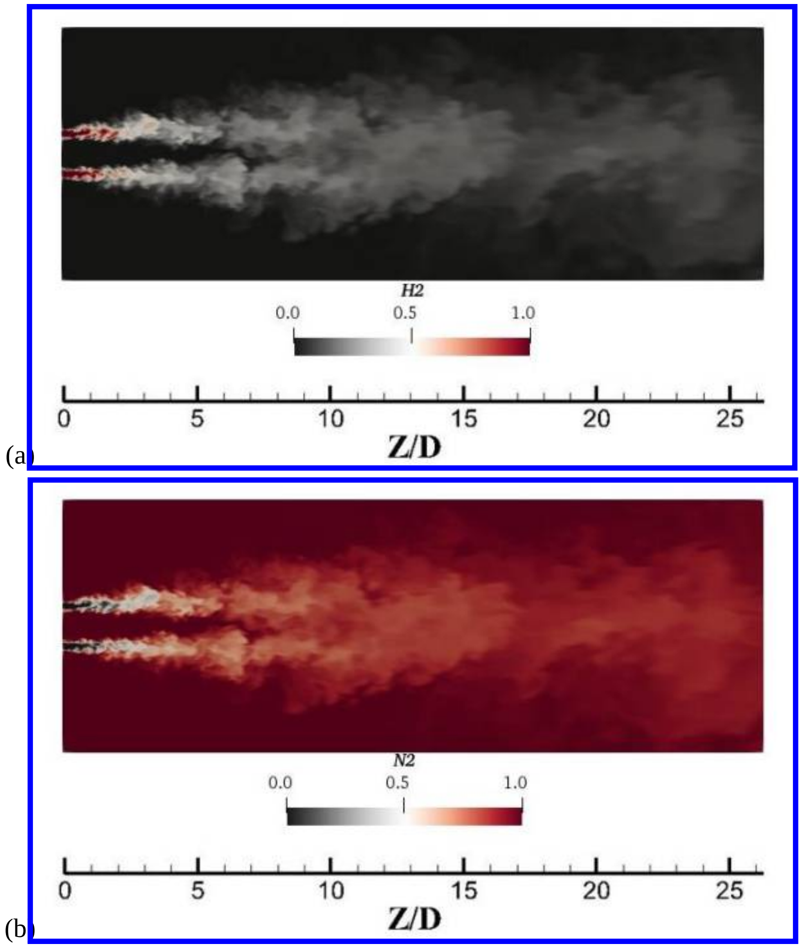

Figure 6. Instantaneous mass fraction distribution of (a) hydrogen and (b) nitrogen on the centerplane

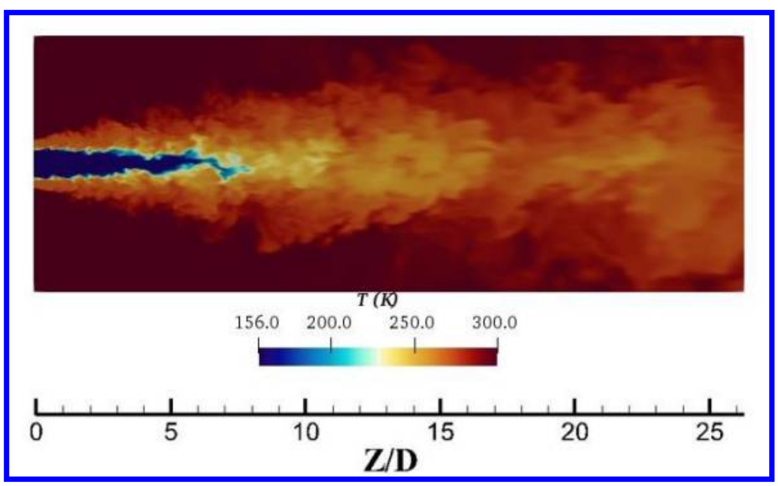

Figure 7. Instantaneous temperature distribution on the centerplane

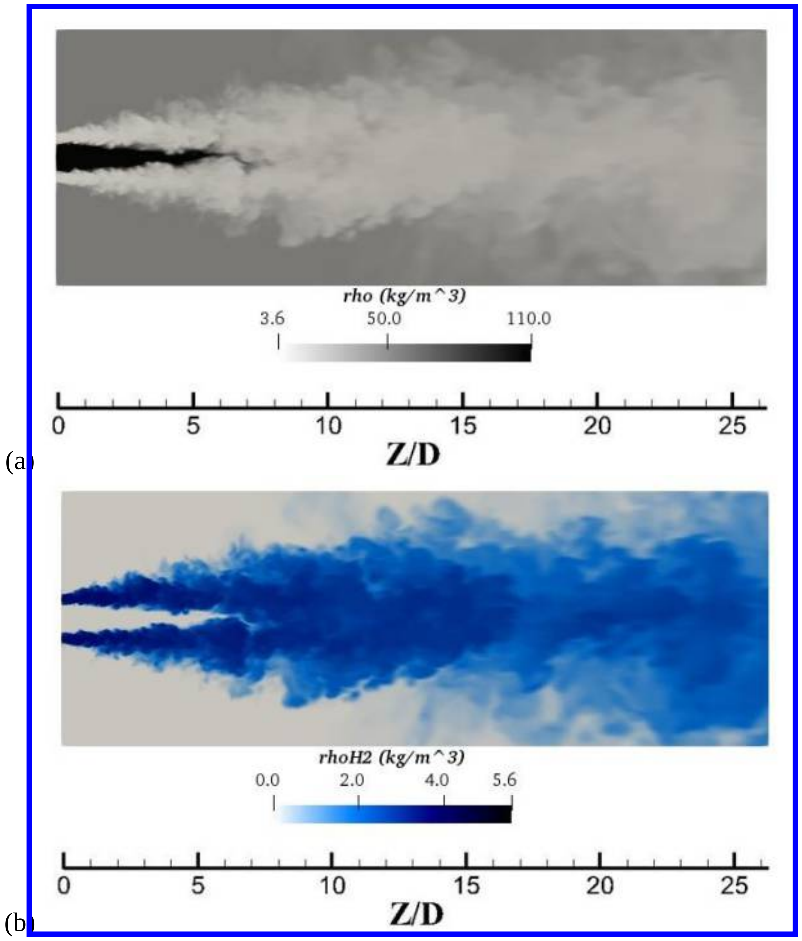

Figure 8. Instantaneous contours of (a) density and (b) hydrogen density on the centerplane

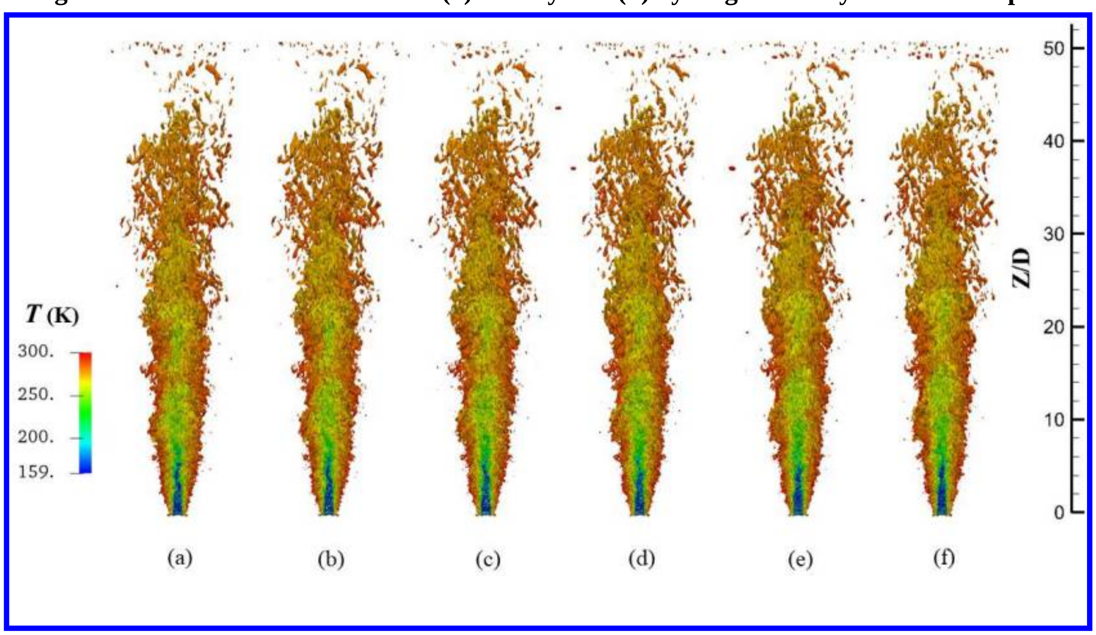

Figure 9. Vortex structures represented by iso-surfaces of Q-criterion (the second invariant of the velocity gradient tensor, an iso value of 5×10^{6} s^{-2} is used) colored by temperature with a time interval of 1×10^{-4} s

From the distribution of the density magnitude in Figure 10, the jet boundary can be visually identified. The cold nitrogen jet differentiates with the surrounding warm hydrogen jet due to both temperature and molecular weight differences, while the warm hydrogen jet differentiates with the surrounding nearly equal-temperature nitrogen gas due simply to the molecular weight difference. Thus it can be said that the large density gradient marks the boundaries of the nitrogen and hydrogen jets during the initial expanding stage. During the drastic heating process, the width of the jet flow expands nearly double, which drives the flow itself to a very high speed temporally. In the modeling, an instantaneous flow speed close to the sonic speed can even be observed. Accordingly, the local time step is significantly constrained by the maximum CFL number, namely the stiff phase-change phenomenon. The jet width initially expands nearly linearly until around Z=20D, then isobar mixing occurs. Purely heat exchange does not smear the large density gradient because of the large difference in the molecular weights of nitrogen and hydrogen. With the further proceeding of the mixing process, the hydrogen mixed with the surrounding nitrogen gas and the enveloped nitrogen jet, which obscures the plume boundary gradually in the downstream after through a region in the shape of a mushroom cap. Such a mushroom cap is more clearly seen in the early jet development as in Figure 10 (a) and then evolve into a larger one in the quasi-steady stage. The formation of the mushroom-cap region indicates that the thermal expansion rate of nitrogen jet has a sudden increase due to the breakup of the jet potential core. The drastic expansion obviously increases transverse velocity, which causes the obvious increase in the width of the jet flow. Correspondingly the streamwise flux reduces, thus forming a mushroom-cap region in the downstream plume. Exactly the top of the cap corresponds to the location of the waist-like region. After this sudden expansion region, the mixing driven by expansion becomes weak as the plume temperature is close to the surrounding gas, and the mixing afterward is dominated by turbulent diffusion.

(a)

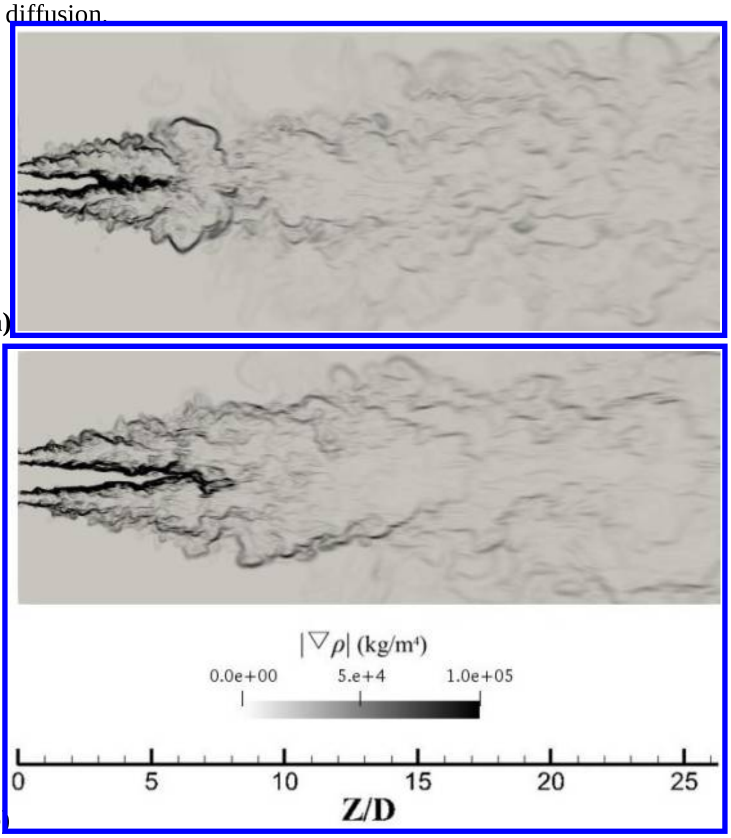

(b)

Figure 10. Contours of density magnitude in (a) an early jet development state and (b) the quasi-steady stage

From the streamlines in Figure 11 (a), the flow turns transversely at the location corresponding to the sudden expansion region at around Z=7D. The flow turning and back subsequently forms a recirculation zone, which then induces a more obvious flow turning and back. It is the first flow back causes the waist-like region in Figure 10 (a). The second flow turning and back does not leave an imprint on the fields of density magnitude, possibly because the fully mixed obscures the jet boundary. In Figure 11 (b), there is mild flow turning towards the transverse direction from Z=7D to 17D, after which the flow turns back towards the axis to form the top of the cap region in Figure 10 (b). The mild turning and back in Figure 11 (b) does not induce any observable recirculation zone.

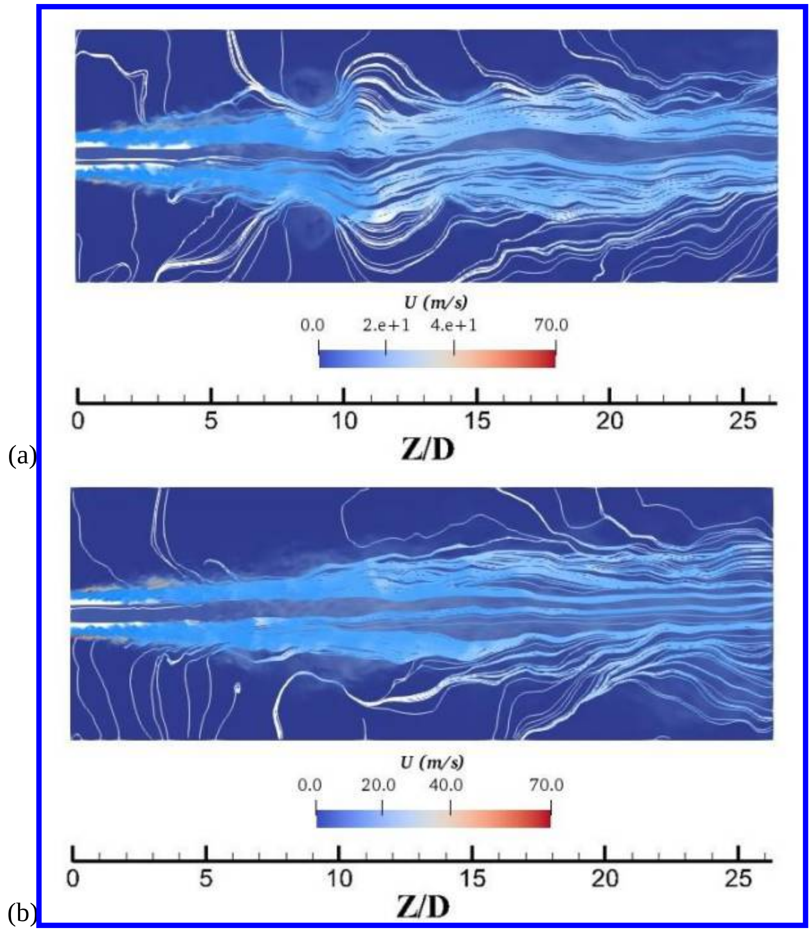

Figure 11. Streamlines overlaid on the velocity magnitude field in (a) the early jet development state and (b) the quasi-steady stage

Conclusions

In this study, a supercritical GN_2/GH_2 jet has been modeled by using the ECS method in the framework of large eddy simulation. The verification of the real-gas thermodynamics properties for a binary N_2/H_2 mixture at p=4 MPa against the standard data shows the accuracy of ECS method is superior to the PR-EOS model. A hydrid pressure/density solver is developed to model the high-speed flow caused by the sudden volume expansion of a heated flow in case of the stiff phase-change phenomenon. The solver will automatically select the density-based or pressure-based mode adapting to the local maximum Mach number within the divided zone. Grid convergence study under a series of mesh resolutions from 9.6 to 20.02 million cells shows that the current mesh with 20.02 million cells has achieved grid independence. In comparison with the experimental data, the current prediction nearly doubly overpredicts the potential core of the nitrogen jet, while agrees better in the fully mixing region. The main core of the nitrogen jet persists until around Z=6*D*, before which the mixing between the hydrogen and the nitrogen is dominated by the small eddies arisen from the shear stress. After Z=6*D* and within a short axial distance of 2D, the nitrogen jet breaks up into discrete "droplet-shape" regions, which then quickly vanished. The nitrogen jet core measured from the density field is thinner than that delimited by a critical temperature, indicating that the thermal diffusion is faster than the species diffusion and the non-unity Lewis number effect should be considered in this case. From the hydrogen density distribution, the waist-like region can be clearly identified as a relatively higher density overlaid on a lower density region. The waist-like region exists in all the sequent evolvement of vortex structures and thus is not an instantaneous phenomenon.

During the drastic heating process, the width of the jet flow expands nearly double, which drives the flow itself to a very high speed temporally. In the modeling, an instantaneous flow speed close to the sonic speed can even be observed. Accordingly, the local time step is significantly constrained by the maximum CFL number, namely the stiff phase-change phenomenon. A mushroom-cap region is formed when the thermal expansion rate of nitrogen jet has a sudden increase due to the breakup of the jet potential core. The drastic expansion obviously increases transverse velocity, which causes an obvious increase in the width of the jet flow. The streamlines indicate that the flow turns transversely at the location corresponding to the sudden expansion region, and it is the backflow causes the shrinking waist-like region.

Acknowledgments

The project was supported by the Training Program of the Major Research Plan of the National Natural Science Foundation of China (Grant No. 91641110), the Open founding of National Key Laboratory of Science and Technology on Aero-Engine Aero-Thermodynamics (Grant No. 6142702180307), and LHD Innovative Foundation (Grant No. LHD2018JS01). The authors are also grateful to the National Supercomputer Center in Tianjin for providing the computational resource.

References

1. Müller, H., Pfitzner, M., Matheis, J., and Hickel, S., "Large-Eddy Simulation of Coaxial Ln2/Gh2 Injection at Trans- and Supercritical Conditions," *Journal of Propulsion and Power*, 2015, pp. 1-11. doi: 10.2514/1.B35827
2. Won-Wook, K., and Suresh, M., "A New Dynamic One-Equation Subgrid-Scale Model for Large Eddy Simulations," *33rd Aerospace Sciences Meeting and Exhibit*, Reno, NV, January 9-12, 1995. doi: 10.2514/6.1995-356
3. Yoshizawa, A., "Statistical Theory for Compressible Turbulent Shear Flows, with the Application to Subgrid Modeling," *The Physics of Fluids,* Vol. 29, No. 7, 1986, pp. 2152-2164. doi: 10.1063/1.865552
4. Chakravarthy, V., and Menon, S., "Large-Eddy Simulation of Turbulent Premixed Flames in the Flamelet Regime," *Combustion Science and Technology,* Vol. 162, No. 1, 2001, pp. 175-222. doi: 10.1080/00102200108952141
5. Fureby, C., "LES for Supersonic Combustion." AIAA 2012-5979, 24-28 September 2012. doi: 10.2514/6.2012-5979
6. Fureby, C., Tabor, G., Weller, H. G., and Gosman, A. D., "A Comparative Study of Subgrid Scale Models in Homogeneous Isotropic Turbulence," *Physic of Fluids,* Vol. 9, 1997, pp. 1416-1429. doi: 10.1063/1.869254
7. Fureby, C., Gosman, A. D., Tabor, G., Weller, H. G., N. Sandham, U. o. S., Southampton, and Wolfshtein, M., "Large Eddy Simulation of Turbulent Channel Flows," *In Proceedings of Turbulent Shear Flows 11,* Vol. 3, 1997, pp. 28-33.
8. Li, X., Yao, W., and Fan, X., "Large-Eddy Simulation of Time Evolution and Instability of Highly Underexpanded Sonic Jets," *AIAA Journal,* Vol. 54, No. 10, 2016, pp. 3191-3211. doi: 10.2514/1.J054689
9. Smagorinsky, J., "General Circulation Experiments with the Primitive Equations. I. The Basic Experiment," *Monthly Weather Review,* Vol. 91, 1963, pp. 99–164. doi: 10.1175/1520-0493(1963)0912.3.CO;2
10. Kim, S.-E., "Large Eddy Simulation Using an Unstrcutured Mesh Based Finite-Volume Solver." AIAA 2004-2548, 28 June - 1 July 2004. doi: 10.2514/6.2004-2548
11. Kim, W.-W., Menon, S., Kim, W.-W., and Menon, S., "Application of the Localized Dynamic Subgrid-Scale Model to Turbulent Wall-Bounded Flows," 1997. doi: 10.2514/6.1997-210
12. Liu, S., Meneveau, C., and Katz, J., "On the Properties of Similarity Subgrid-Scale Models as Deduced from Measurements in a Turbulent Jet," *Journal of Fluid Mechanics,* Vol. 275, 1994, pp. 83-119. doi: 10.1017/S0022112094002296
13. Weller, H. G., Tabor, G., Jasak, H., and Fureby, C., "A Tensorial Approach to CFD Using Object Oriented Techniques," *Computers in Physics,* Vol. 12, No. 6, 1997, pp. 620-631. doi: 10.1063/1.168744
14. Kurganov, A., and Tadmor, E., "New High-Resolution Central Schemes for Nonlinear Conservation Laws and Convection–Diffusion Equations," *Journal of Computational Physics,* Vol. 160, No. 1, 2000, pp. 241-282. doi: 10.1006/jcph.2000.6459
15. Vuorinen, V., Larmi, M., Schlatter, P., Fuchs, L., and Boersma, B. J., "A Low-Dissipative, Scale-Selective Discretization Scheme for the Navier–Stokes Equations," *Computers & Fluids,* Vol. 70, 2012, pp. 195-205. doi: 10.1016/j.compfluid.2012.09.022
16. Baba-Ahmadi, M. H., and Tabor, G., "Inlet Conditions for LES Using Mapping and Feedback Control," *Computers & Fluids,* Vol. 38, No. 6, 2009, pp. 1299-1311. doi: 10.1016/j.compfluid.2009.02.001
17. Wu, K., Li, X., Yao, W., and Fan, X., "Three-Dimensional Numerical Study of the Acoustic Properties of a Highly Underexpanded Jet." AIAA 2015-3572, 6-9 July 2015. doi: 10.2514/6.2015-3572
18. Li, X., Wu, K., Yao, W., and Fan, X., "A Comparative Study of Highly Underexpanded Nitrogen and Hydrogen Jets Using Large Eddy Simulation." AIAA 2015-3573, 6-9 July 2015. doi: 10.2514/6.2015-3573
19. Greenshields, C. J., Weller, H. G., Gasparini, L., and Reese, J. M., "Implementation of Semi-Discrete, Non-Staggered Central Schemes in a Colocated, Polyhedral, Finite Volume Framework, for High-Speed Viscous Flows," *International Journal for Numerical Methods in Fluids,* Vol. 38, No. 2, 2009, pp. 139-161. doi: 10.1002/fld.2069
20. Li, X., Zhou, R., Yao, W., and Fan, X., "Flow Characteristic of Highly Underexpanded Jets from Various Nozzle Geometries," *Applied Thermal Engineering,* Vol. 125, 2017, pp. 240-253. doi: 10.1016/j.applthermaleng.2017.07.002
21. Li, X., Fan, E., Yao, W., and Fan, X., "Numerical Investigation of Characteristic Frequency Excited Highly Underexpanded Jets," *Aerospace Science and Technology,* Vol. 63, 2017, pp. 304-316. doi: 10.1016/j.ast.2017.01.005

22. Lee, Y., Yao, W., and Fan, X., "A Low-Dissipation Solver Based on Openfoam Designed for Large Eddy Simulation in Compressible Flows." AIAA 2017-2444, 6-9 March 2017. doi: 10.2514/6.2017-2444
23. Li, X., Wu, K., Yao, W., and Fan, X., "A Comparative Study of Highly Underexpanded Nitrogen and Hydrogen Jets Using Large Eddy Simulation," *International Journal of Hydrogen Energy,* Vol. 41, No. 9, 2015, pp. 5151-5161. doi: 10.1016/j.ijhydene.2016.01.120
24. Yao, W., Lu, Y., Wu, K., Wang, J., and Fan, X., "Modeling Analysis of an Actively Cooled Scramjet Combustor under Different Kerosene/Air Ratios," *Journal of Propulsion and Power,* Vol. 34, No. 4, 2018, pp. 975-991. doi: 10.2514/1.B36866
25. Wu, K., Yao, W., and Fan, X., "Development and Fidelity Evaluation of a Skeletal Ethylene Mechanism under Scramjet-Relevant Conditions," *Energy & Fuels,* Vol. 31, No. 12, 2017, pp. 14296-14305. doi: 10.1021/acs.energyfuels.7b03033
26. Yao, W., Wang, J., Lu, Y., Li, X., and Fan, X., "Full-Scale Detached Eddy Simulation of Kerosene Fueled Scramjet Combustor Based on Skeletal Mechanism." AIAA 2015-3579, 6-9 July 2015. doi: 10.2514/6.2015-3579
27. Wu, K., Zhang, P., Yao, W., and Fan, X., "Numerical Investigation on Flame Stabilization in Dlr Hydrogen Supersonic Combustor with Strut Injection," *Combustion Science and Technology,* Vol. 189, No. 12, 2017, pp. 2154-2179. doi: 10.1080/00102202.2017.1365847
28. Yao, W., Lu, Y., Li, X., Wang, J., and Fan, X., "Improved Delayed Detached Eddy Simulation of a High-Ma Active-Cooled Scramjet Combustor Based on Skeletal Kerosene Mechanism." AIAA-2016-4761, 25-27 July 2016. doi: 10.2514/6.2016-4761
29. Yao, W., Yuan, Y., Li, X., Wang, J., Wu, K., and Fan, X., "Comparative Study of Elliptic and Round Scramjet Combustors Fueled by RP-3," *Journal of Propulsion and Power,* Vol. 34, No. 3, 2018, pp. 772-786. doi: arc.aiaa.org/doi/abs/10.2514/1.B36721
30. Yao, W., Lu, Y., Wu, K., Wang, J., and Fan, X., "Modeling Analysis of an Actively-Cooled Scramjet Combustor under Different Kerosene/Air Ratios," *Journal of Propulsion and Power,* Vol. 34, No. 4, 2018, pp. 975-991. doi: doi.org/10.2514/1.B36866
31. Yao, W., Wu, K., and Fan, X., "Influences of Domain Symmetry on Supersonic Combustion Modeling," *Journal of Propulsion and Power,* Vol. 35, No. 2, 2019, pp. 451-465. doi: 10.2514/1.B37227
32. Kennedy, C. A., and Gruber, A., "Reduced Aliasing Formulations of the Convective Terms within the Navier–Stokes Equations for a Compressible Fluid," *Journal of Computational Physics,* Vol. 227, 2008, pp. 1676–1700. doi: 10.1016/j.jcp.2007.09.020